Obrabotka metallov (tekhnologiya, oborudovanie, instrumenty) = Metal Working and Material Science. 2026 vol. 28 no. 2 pp. 6–31
ISSN: 1994-6309 (print) / 2541-819X (online)
DOI: 10.17212/1994-6309-2026-28.2-6-31

NSTU NETI

Obrabotka metallov - Metal Working and Material Science

Journal homepage: http://journals.nstu.ru/obrabotka_metallov

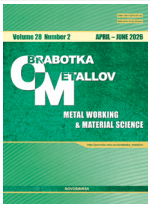

# Dependence of gas porosity in a metal-polymer composite on residual pressure during vibro-vacuum degassing for metal-composite tool bodies

***Nikolay Lubimyi*** [a], ***Andrey Polshin*** [b], ***Boris Chetverikov*** [c, *], ***Vladislav Prokopenko*** [d], ***Ardalion Maltsev*** [e], ***Mikhail Bytsenko*** [f]

Belgorod State Technological University named after V.G. Shukhov, 46 Kostyukova St., Belgorod, 308012, Russian Federation

[a] https://orcid.org/0000-0002-6131-3217, nslubim@bk.ru; [b] https://orcid.org/0000-0001-5809-4458, info@polshin.ru;
[c] https://orcid.org/0000-0003-1801-6767, await_rescue@mail.ru; [d] https://orcid.org/0000-0002-7120-1411, vlad.prokopenko1@yandex.ru;
[e] https://orcid.org/0000-0002-0878-3658, ardalion_bgtu@mail.ru; [f] https://orcid.org/0009-0004-2133-885X, b.michutka2005@gmail.com

**ARTICLE INFO**

*Article history*:
Received: 02 February 2026
Revised: 12 February 2026
Accepted: 14 March 2026
Available online: 15 June 2026

*Keywords*:
Metal–composite technology
Metal–polymer composite material
Vibro-vacuum degassing
Gas porosity
*SLM* shell

*Funding*
This study was supported by grant No. 23-79-10022 from the Russian Science Foundation, https://rscf.ru/project/23-79-10022/.

*Acknowledgements*
The study was performed using the facilities of the High Technologies Center of Belgorod State Technological University named after V.G. Shukhov.

**ABSTRACT**

**Introduction.** The metal–composite technology (*MCT*) for manufacturing tool bodies using an "*SLM* shell + metal–polymer composite material (Metal–polymer/*MPCM*)" enables the implementation of curvilinear coolant/lubricant supply channels and reduces the additively manufactured metal volume; however, the quality of filling thin-walled cavities is critically determined by the level of gas porosity of the filler. Gas porosity degrades the thermal conductivity and load-bearing capacity of the *MPCM*, reduces the stability of filling in critical zones near the *SLM* shell wall and adjacent to the channels, and increases properties dispersion and the risk of defects during tool operation. ***The purpose of the work*** is to experimentally establish the relationship between *MPCM* gas porosity and residual pressure under vibro-vacuum degassing and to justify a technologically preferable vacuum range for application in *MCT* tool bodies. **Methodology.** The study was carried out using a vibro-vacuum setup comprising a preliminary degassing chamber and a casting chamber with low-frequency vibration. Standard *MPCM* samples were produced for each vacuum condition. Porosity was evaluated using an adopted scoring scale based on microscopy (analysis of pore distribution, clustering, and characteristic defect sizes). **Results and discussion.** The experiment revealed a stable nonlinear (*V*-shaped) trend: as pressure decreases from atmospheric to approximately 450 Pa, the average porosity score monotonically decreases and reaches a minimum in the 400–350 Pa range (1–2 points). Further vacuum intensification below 300 Pa leads to vigorous gas evolution and foaming ("boiling"), accompanied by a sharp increase in defectiveness (up to 3–5 points). ***Conclusions.*** The identified optimal vacuum range of 400–350 Pa is recommended as a compromise between effective removal of entrapped gas and avoidance of the foaming, ensuring reproducible filling quality of *MPCM* within *SLM* shells in *MCT* tool-bodies manufacturing.

**For citation:** Lubimyi N.S., Polshin A.A., Chetverikov B.S., Prokopenko V.S., Maltsev A.K., Bytsenko M.V. Dependence of gas porosity in a metal-polymer composite on residual pressure during vibro-vacuum degassing for metal-composite tool bodies. *Obrabotka metallov (tekhnologiya, oborudovanie, instrumenty) = Metal Working and Material Science*, 2026, vol. 28, no. 2, pp. 6–31. DOI: 10.17212/1994-6309-2026-28.2-6-31. (In Russian).

*** Corresponding author**
*Chetverikov Boris S.,* Ph.D. (Engineering), Associate Professor
Belgorod State Technological University named after V.G. Shukhov,
46 Kostyukova St.,
308012, Belgorod, Russian Federation
**Tel.:** +7 951 134-32-43, **e-mail:** await_rescue@mail.ru

## Introduction

In tool manufacturing, there is a growing demand for tool bodies with functionally integrated internal channels for supplying coolant/lubricant technological media (*CLTM*), which enable improved thermal conditions and cutting stability. The most promising approach for implementing channels of complex spatial geometry is additive manufacturing (*SLM* and related processes), which provides curvilinear channels, smooth cross-sectional transitions, and flow orientation toward the functional zones of the cutting part [1–3]. However, all-metal additive manufacturing of cutting tool bodies often proves economically unfeasible due to increased build volume and post-processing requirements. Therefore, hybrid solutions are of practical interest, in which the additive part is made as a thin-walled *SLM* shell forming mounting and reference surfaces, as well as *CLTM* channels, while the internal volume is filled with a metal–polymer composite material (*MPCM*). This "*SLM* shell + *MPCM*" architecture belongs to metal–composite technology (*MCT*) and allows reducing the additive metal volume while maintaining the shell's functionality.

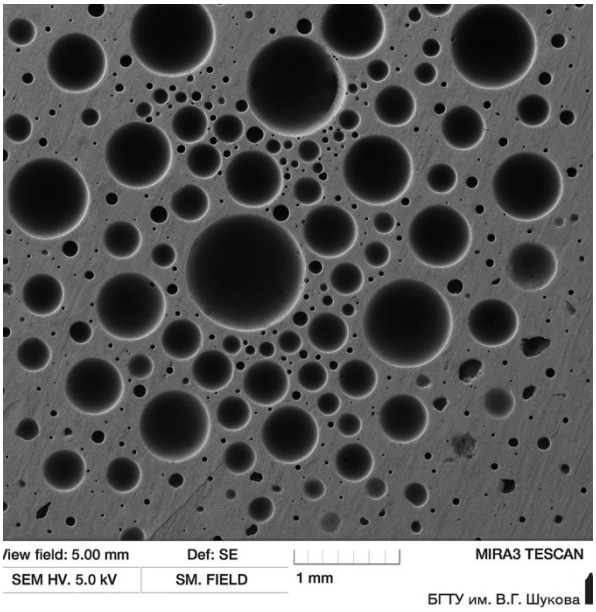


*Fig. 1.* Microstructure of a metal–polymer composite sample obtained by casting without degassing, at a pressure 101,325 Pa (region of gas inclusion concentration)

The quality of filling internal cavities of *SLM* shells is largely determined by the gas porosity of *MPCM* (Fig. 1), which arises due to air entrapment during preparation and casting of the viscous filled composition. Pores degrade the effective thermal conductivity of the composite [4] and can reduce the load-bearing capacity of the infill; defects are particularly critical in the 'shell–MPCM" contact zone and near the *CLTM* channels. Therefore, *MPCM* degassing is a mandatory stage in the technological route of *MCT* tool bodies and should be considered not abstractly, but through acceptance criteria for tool bodies (acceptable porosity level and absence of large defects in critical zones). In earlier studies, it was noted that samples cured at atmospheric pressure exhibit microscopic defects (up to millimeter sizes), whereas the application of vacuuming allows virtually eliminating visible pores [5].

Vacuuming and degassing are widely used in composite manufacturing technologies, and several studies have shown that the efficiency of removing entrapped/dissolved gases significantly depends on the level of residual pressure [6–8]. However, for viscous filled systems and for cases of filling closed cavities of complex geometry, practical uncertainty remains: what vacuum level is sufficient to reduce porosity, and at what point lies the threshold beyond which further vacuum intensification may lead to undesirable gas evolution and foaming of the composition. An additional technological tool is vibration assistance, which promotes bubble escape and improves fillability. However, vacuum and vibration conditions must be selected in a coordinated and substantiated manner.

Thus, an unresolved task for metal-composite tool bodies is the experimentally confirmed determination of the residual pressure range that ensures minimum *MPCM* gas porosity without transitioning into the foaming regime, and the formalization of technological acceptance criteria. An additional complexity in the case of *MCT* is that filling is performed not into a flat or open laminate, but into internal cavities of a shell with complex geometry, where there are thin-walled sections, narrow partitions, extended channels, and local volumes prone to bubble retention. Therefore, in practice, a combined effect is applied: vacuuming + vibration assistance, which increases fluidity and promotes bubble escape. For processes similar in physics (vacuum infusion, molding), it has been shown that vibration can affect void content and impregnation quality. There are studies analyzing the effect of vibration assistance on porosity and strength characteristics of composites during vacuum processing [9, 10]. These results are methodologically important for *MCT*.

Although materials and geometry differ, the very idea of "controlled rheology" combined with facilitated degassing through vibration and vacuum has a common physical basis.

In practice (Fig. 2), it has been established that during preparation and transportation of viscous filled *MPCM*, gas inclusions form almost inevitably (rheology, mixing, casting ); therefore, preliminary degassing is considered a mandatory stage of the vibro-vacuum filling process [11].


*Fig. 2.* Experimental setup for vibro-vacuum filling of internal cavities in *SLM* shells with a metal–polymer composite material (*MPCM*):

1 – vacuum chamber for preliminary degassing; 2 – vibration table; 3 – vacuum chamber for *MPCM* casting into the cavities of *SLM* shells; 4 – hollow *SLM* drill body; 5 – vibrators; 6 – holder (fixture) for producing *MPCM* samples for porosity evaluation

Simultaneously, it has been shown that vibration assistance parameters must ensure increased fluidity without phase separation and foaming. Similar effects and limitations of vibration-assisted vacuum processing are described in references [12, 13]. Within the framework of this study, a frequency range of 40–60 Hz and amplitudes of 0.2–0.6 mm were experimentally established as providing minimum mold filling time and are suitable for further research on the effect of vacuum on porosity.

According to the authors, from a practical perspective, the significance of this work is determined by the fact that degassing sets the "default quality" for the entire *MCT*: defects formed during the *MPCM* preparation/degassing stage cannot be eliminated by subsequent operations and manifest as hidden filling inhomogeneity. In tool bodies, this is particularly critical because it is the filling quality that determines the operational stability of the composite structure and the reproducibility of the performance effect.

***The purpose of this research*** is to experimentally determine the relationship between *MPCM* gas porosity and residual pressure during vibro-vacuum degassing and to justify a technologically preferable vacuum range for application in *MCT* cutting tool bodies, oriented toward import substitution and small-scale production conditions. To achieve this purpose, the following *tasks* were accomplished:

– to adapt the porosity evaluation methodology and *MPCM* acceptance criteria for application to *MCT* tool bodies;

– to conduct a series of experiments at various residual pressure values with the production of parallel specimens;

– to identify the "pressure–porosity" pattern and determine the optimal and critical parameter regions corresponding to technological limitations of *SLM* shell filling.

## Methods

The object of this study is a metal–polymer composite used in metal–composite technology (*MCT*) for filling internal cavities of thin-walled *SLM* shells of tool bodies (in particular, bodies of modular drills with internal *CLTM* supply channels). Degassing is considered a mandatory stage in the *MCT* technological

route, aimed at reducing gas porosity, stabilizing the filling of thin-walled zones, and minimizing defects near the *SLM* shell wall and adjacent to the *CLTM* channels (the critical "metal–MPCM" contact zone).

Degassing and filling were performed using a specialized vibro-vacuum setup (Fig. 2), providing:

– preliminary vacuum degassing of *MPCM* before casting;

– vibration-assisted casting of *MPCM* into the *SLM* shell cavities under reduced pressure;

– production of reference *MPCM* specimens for subsequent porosity evaluation under identical conditions.

The technological sequence included: preparation of a specialized fixture (Fig. 3) for simultaneous production of 5 specimens, *MPCM* preparation, vacuuming and filling of the fixture cavities at a specified pressure value with simultaneous low-frequency vibration exposure, holding, and further curing of the material.

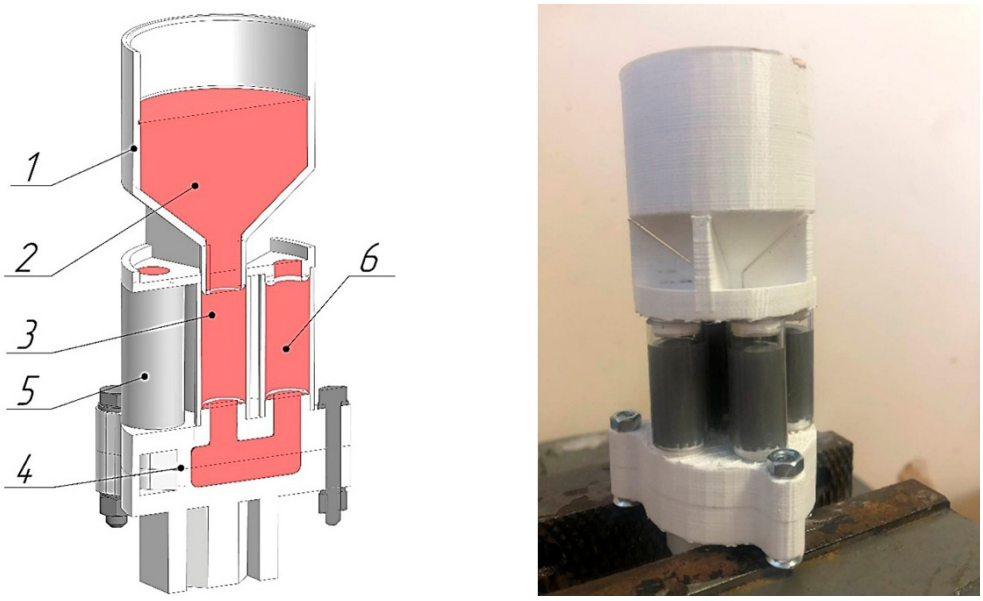


*a* *b*

*Fig. 3.* Equipment for producing *MPCM* samples for the porosity rating assessment:

*a* – digital model of the equipment, where 1 – reservoir, 2 – *MPCM*, 3 – sprue, 4 – distributor, 5 – mould, 6 – *MPCM* sample; *b* – physical model of the equipment filled with *MPCM* (101,325 Pa)

The experiment was aimed at establishing the relationship between *MPCM* gas porosity and the applied vacuum level during vibro-vacuum degassing. The primary variable factor was the residual pressure in the vacuum chamber ("vacuum level"). To eliminate the influence of extraneous factors, the following parameters were fixed:

– *MPCM* composition and its preparation regime;

– geometry of the mold for reference specimens;

– vibration regime (frequency, amplitude, duration);

– temperature conditions of the process and holding.

A two-component metal–polymer composite material "Ferro-Chrome" (*TU 2257-002-48460567-00*) [11] was used as the studied filling material. In this study, the "yellow (liquid)" activator and the manufacturer's diluent were used. The composition belongs to the class of metal–polymers (base component + activator) intended for repair and restoration operations and cast filling of cavities, subject to compliance with preparation and degassing regimes. The specified technological and physical-mechanical characteristics of the *MPCM* used, affecting the vacuuming conditions and porosity formation, are presented in Table 1.

The detailed formulation (mass fractions of individual components, type of binder/curing agent, filler grain size distribution) is not disclosed in the open part of the technical documentation available

Table 1

**Passport technological and physical-mechanical characteristics of Ferro-Chrome *MPCM* (according to the manufacturer)**

| Parameter | Value | Note |
|---|---|---|
| Specific gravity (density) of the composition, g/cm$^3$ | 2.5 | for the “yellow” activator |
| Pot life at (18–20) °C, min | 45 | for the “yellow” activator |
| *Vicat* heat resistance, °C | 300 | according to manufacturer’s data |
| Operating temperature, °C | From −120 to +170 | for the “yellow” activator |
| Curing time at 20 °C until machining, h | 3.5–4 | according to manufacturer’s data |
| Curing time at 20 °C until full strength, h | 24 | according to manufacturer’s data |
| *Brinell* hardness, MPa | 310 | according to manufacturer’s data |
| Compressive strength, MPa | 230 | according to manufacturer’s data |
| Flexural strength, MPa | 76 | according to manufacturer’s data |
| Adhesive strength (normal pull-off) to steel, MPa | 45 | according to manufacturer’s data |
| Adhesive strength (normal pull-off) to aluminum, MPa | 45 | according to manufacturer’s data |
| Adhesive strength (normal pull-off) to brass, MPa | 44 | according to manufacturer’s data |

to the authors. In this regard, the specified characteristics of the material are provided in this study, and the technological conditions of preparation, degassing, and curing are strictly fixed (component ratio, temperature, time, residual pressure, vibration regime), which ensures the reproducibility of the experiment at the technological process level.

Mixing was performed at a temperature of 18–20 °C. The “base” and “activator (yellow, liquid)” components were dosed and mixed in accordance with the manufacturer’s recommendations for the “Ferro-Chrome” material [11] in the following weight proportions: base 19.5 g / activator “yellow” (liquid) 1 g / diluent 1 g. Subsequently, preliminary vacuum degassing was performed according to the regime described below.

*Fig. 4.* The process of mechanical mixing of *MPCM* components

It should be noted that *MPCM* [11] is often a repair material. The manufacturer recommends applying *MPCM* in thin layers precisely due to the risk of gas-air inclusion accumulation. Mixing of components is recommended using a special spatula with low intensity. However, a technological difficulty arises when preparing significant volumes of *MPCM*, as effective mixing without the use of mechanized mixers will not allow proper blending of components before the onset of the polymerization process and the loss of fluidity. Therefore, mechanical stirrers (Fig. 4) were used when preparing industrial volumes of *MPCM* for casting purposes, as a result of which the *MPCM* was intensively saturated with gaseous inclusions. This is clearly visible in the microscopy results of specimens cured under conditions close to atmospheric pressure.

For quantitative evaluation of gas porosity, reference *MPCM* specimens were produced under conditions identical to those used for filling *SLM* shells. The specimens were molded in a special holder/fixture (position **5** in Fig. 3), which enabled: reproducible fixation of specimen geometry; ensuring comparability of degassing and casting conditions; and performing identical surface preparation for microscopy and pore analysis.

For each residual pressure value in the vacuum chamber, a series of $\boldsymbol{n} = 5$ parallel *MPCM* specimens was simultaneously produced using the fixture (Fig. 3). After curing, mechanical specimen preparation was performed: cutting and grinding.

The gas porosity evaluation methodology was carried out using a combined approach, including:

– visual rating assessment. After specimen preparation, on each of the 5 obtained specimens, it was possible to visually select the zone of the studied specimen that had the highest number of defects in the area of investigation. As a rule, this is the bottom zone of the specimen, where the largest amount of gas inclusions is accumulated, migrating from the distributor zone (position **4**, Fig. 3). This zone is the most susceptible to porosity accumulation due to the specifics of the fixture geometry.

– microscopic analysis (the main control tool). Microscopy of prepared surfaces of the most defective zone (5 × 5 mm) was performed with image registration on a field-emission scanning electron microscope *TESCAN MIRA 3 LMU*, at fixed magnification and identical illumination/contrast settings. Imaging was performed in secondary electron (*SE*) detection mode at an accelerating voltage of 5.0 kV and a working distance ***WD*** ≈ 10 mm. For the micrographs presented in this study, the field of view was 5.00 mm, with a scale of 1 mm.

Subsequently, the following parameters were evaluated: the area fraction of pores in the selected field of view (***P***, %); the pore size distribution (*d_max*, mm); and the porosity character (single pores, clusters, porous zones, pores at the "shell–infill" boundary, etc.)

The mean porosity score for each regime was calculated as:

$$\bar{x} = \frac{1}{n}\sum_{i=1}^{n} x_i \,, \tag{1}$$

where $\boldsymbol{x_i}$ is the porosity score of the ***i***-th specimen; ***n*** = 5.

The scatter was evaluated using the sample standard deviation:

$$s = \sqrt{\frac{\sum_{i=1}^{n}(x_i - \underline{x})^2}{n-1}} \,, \tag{2}$$

The 95 % confidence interval (*CI*) for the mean value was determined using the ***t***-distribution:

$$\Delta 95 = t_{0.975,n-1} \cdot \frac{s}{\sqrt{n}} \,, \tag{3}$$

where $t_{0.975,\,n\text{-}1} = 2.776$ for $n = 5$.

The values of $\boldsymbol{x_i}$ and **Δ**95 are presented in the Table 4 as separate columns, and error bars corresponding to ±**Δ**95 are shown in Fig. 14.

– A microdefect rating scale was developed (Table 2), based on the terminology of cast material defects [14] (for unification of pore/shrinkage cavity description) and on approaches to void content evaluation in composites adopted in polymer composite standards. The rating assessment $x_i$ was determined for each of the five specimens in the series. The selection of the "most defective zone" was performed within each specimen to standardize the analysis field of 5 × 5 mm. This approach corresponds to the generally accepted practice of void content evaluation in polymer composites [15, 16], where void content is considered a key indicator of quality and technological stability.

In the literature on polymer composites [17], it is noted that critical void content levels for acceptance depend on the application and often fall within the range of approximately 1–2 %, while values up to 5% may be permitted for less critical applications. The boundaries for the area fraction of pores ***P*** were selected following the logic of the standard void content indicator for polymer composites. The ranges of 0.5–1–2 % correspond to the transition from low to moderate void content, at which noticeable changes in mechanical characteristics begin to manifest in composite systems, whereas values on the order of several percent are considered critical for property stability. A threshold of 4% was adopted as a conservative rejection level for the studied technology of metal–polymer element manufacturing, since upon reaching this level, pronounced structural inhomogeneity and high variability of results are observed.

An additional criterion of maximum equivalent pore diameter – *d_max* – was introduced, since the same area fraction of pores may correspond to fundamentally different defect hazards (many small pores

Table 2

**Developed microdefect rating scale and acceptance criteria**

| Number of points | Area porosity, % ($\Sigma S_{por} / \Sigma S_{sample}$) | Conditions by size | Acceptability for *MCT* drill bodies |
|---|---|---|---|
| 0 points | no pores detected. < 0.05 % | d_max < 0.30 mm; no clusters | Unconditionally acceptable; no additional actions required |
| 1 points | 0.05–0.5 % | d_max < 0.50 mm; no clusters | Acceptable. Only dispersed porosity is permitted |
| 2 points | 0.5–1.0 % | d_max < 1.00 mm; no clusters | Acceptable with control of defect location by radiographic methods |
| 3 points | 1.0–2.0 % | d_max < 1.50 mm; no clusters | Limitedly acceptable: only for prototype/pre-production trials. Not suitable for serial production |
| 4 points | 2.0–4.0 % | d_max ≤ 2.00 mm; clusters possible | Unacceptable for operation. Permitted only for bench-scale "cold" method development tests. Process adjustment (degassing / vibration / rheology) and re-fabrication required |
| 5 points | > 4.0 % | d_max ≤ 2.00 mm and/or clusters possible | Unconditional rejection. Re-fabrication with correction of vacuum parameters and vibration assistance required |

vs. a single large cavity). For composites, it has been shown [17] that even approximately 1% pore content can noticeably reduce strength characteristics, and large pores are potential stress concentrators and failure initiators. Therefore, *d_max* threshold levels are used as conservative acceptance limits. The *d_max* threshold levels (0.30, 0.50, 1.00, 1.50, 2.00 mm) reflect the transition from dispersed porosity to single large cavities (shrinkage cavities), which are local stress concentrators and indicators of casting technology violations. A *d_max* level ≥ 2.0 mm is adopted as a rejection criterion within the 5×5 mm field, since it corresponds to a large defect comparable in size to the characteristic scale of the control zone.

Clustering is identified as a separate feature, since local pore accumulations are typical of the foaming regime and are technologically more hazardous than uniform dispersed porosity. Clusters lead to local property inhomogeneity, which is particularly critical in the "*SLM* shell–*MPCM*" contact zone and near the *CLTM* channels. A cluster was defined as the presence of at least three pores within a circle with a radius of 0.5 mm. The choice of radius is due to the fact that it corresponds to the local scale of the defective zone (10% of the 5×5 mm field size) and allows the separation of uniform dispersed porosity from local gas accumulation sites. The "≥3 pore" criterion excludes false positives associated with random arrangement of individual pores.

The threshold values were refined based on results from a preliminary series of experiments and were selected to ensure stable separation of processing regimes by defect level with minimal overlap of *P* and *d_max* indicator distributions. Additionally, the consistency of the automated assessment with the scale was confirmed by expert visual classification of micrographs.

To enhance reproducibility and obtain a decimal defect rating, the integral score was calculated based on three quantitative features extracted from micrographs: the area fraction of pores *P*, the maximum equivalent pore diameter *d_max*, and clustering. Linear interpolation was applied within intervals to ensure a continuous assessment. Clustering was defined as the fraction of pores belonging to clusters (≥3 pores within a 0.5 mm radius) and was converted to a scoring scale. The selected thresholds ensure robust separation of degassing regimes: at atmospheric pressure and under excessively deep vacuum, defect severity increases to 4–5 points, whereas in the 350–500 Pa range, minimum values of 1.2–1.9 points are achieved, as confirmed by experimental data.

To automate porosity assessment from micrographs, software (*SW*) named "SEM Porosity Analyzer" was developed in *Python*. The solution is implemented as a locally run interactive web application: computations are performed on the user's computer, while the interface is rendered in the browser. This approach enhances methodological reproducibility (by fixing the set of processing parameters) and makes the tool convenient for routine laboratory work (image loading, visual verification of the pore mask, report export).

*Streamlit* was selected as the user interface framework. Streamlit is a *Python* library for the rapid creation of interactive data analysis applications without developing a dedicated frontend (*HTML/JavaScript*) or building standalone executable *GUI* applications. The interface is generated directly from *Python* code and includes control elements (sliders, toggles, input fields), file upload, and display of images and tables. For porosity assessment tasks, *Streamlit* is advantageous as it allows: rapid configuration of the processing parameter panel; immediate display of intermediate results (*ROI*, threshold, mask, overlay); report saving; and local application launch on any *PC* with *Python* and dependencies installed.

The application is deployed in an isolated environment (*Anaconda*/*venv*) on *Windows 11*, which minimizes the risk of library version conflicts and ensures portability. All image processing and metric calculations are performed using standard open-source computer vision and data analysis libraries. Table 3 lists the key dependencies and their functions within the implemented software.

Table 3

**Software environment and libraries used in the developed tool for automated porosity assessment**

| Component, Library | Function | Use in the developed tool |
|---|---|---|
| *Python* | General-purpose programming language; widely used for scientific computing and data processing | Implements the full processing pipeline: preprocessing, segmentation, pore parameter measurement, and calculation of the integral point score |
| *Streamlit* | Framework for creating interactive data analysis applications with a browser-based interface | Provides the user interface: JPG image upload, parameter panel (calibration, thresholding, morphology, clustering), result visualization, and report export buttons |
| *OpenCV* (cv2) | Computer vision library for image processing (filtering, contrast enhancement, thresholding) | Handles image reading, conversion to grayscale, application of *CLAHE* (local contrast enhancement), and binarization (Otsu/adaptive) |
| scikit-image (skimage.measure, skimage.morphology) | Collection of image analysis and morphological processing algorithms; tools for working with connected components | Performs connected component labeling (pores), calculation of geometric features (area, centroid, equivalent diameter), and mask cleaning (remove_small_objects, closing/opening) |
| scikit-learn (*DBSCAN*) | Machine learning library; *DBSCAN* is a density-based clustering algorithm | Identifies local clusters of pores based on centroid coordinates (eps in mm, min_samples = 3); calculates the proportion of pores within clusters for the clustering component of the final point score |
| *NumPy* | Fundamental library for numerical computing and array operations | Performs fast matrix/mask operations (pixel fraction calculation, coordinate transformations, statistical aggregation) |
| *Pandas* | Tabular data processing (*DataFrame*) and report generation tools | Creates summary tables (Summary) and detailed pore tables (Pores) with parameters for each pore: area, diameter, coordinates, cluster affiliation |
| *openpyxl* | Write-read support for *Excel .xlsx* files | Exports results to *Excel*: separate sheets for Summary (settings and integral metrics) and Pores (parameters of each individual pore) |

To eliminate the influence of service inscriptions or the scale bar, the photograph was cropped to the specimen area. A function for software-based cropping of the lower part of the image to a user-specified fraction of height was also provided. Scaling was ensured based on the measured calibration. For this purpose, the 1 mm scale marker was measured in pixels using the "ruler" tool in a graphics editor. Subsequently, the obtained value for the specific photograph was entered into the "Calibration" field, which allowed converting pixel dimensions to millimeters.

The software is implemented as an interactive window (Fig. 5) divided into a parameter control panel (left) and a results visualization area (right). On the control panel, the user step-by-step specifies the image processing parameters, while the main area simultaneously displays the original and intermediate results, which allows visual control of the pore segmentation correctness before forming the final metrics.

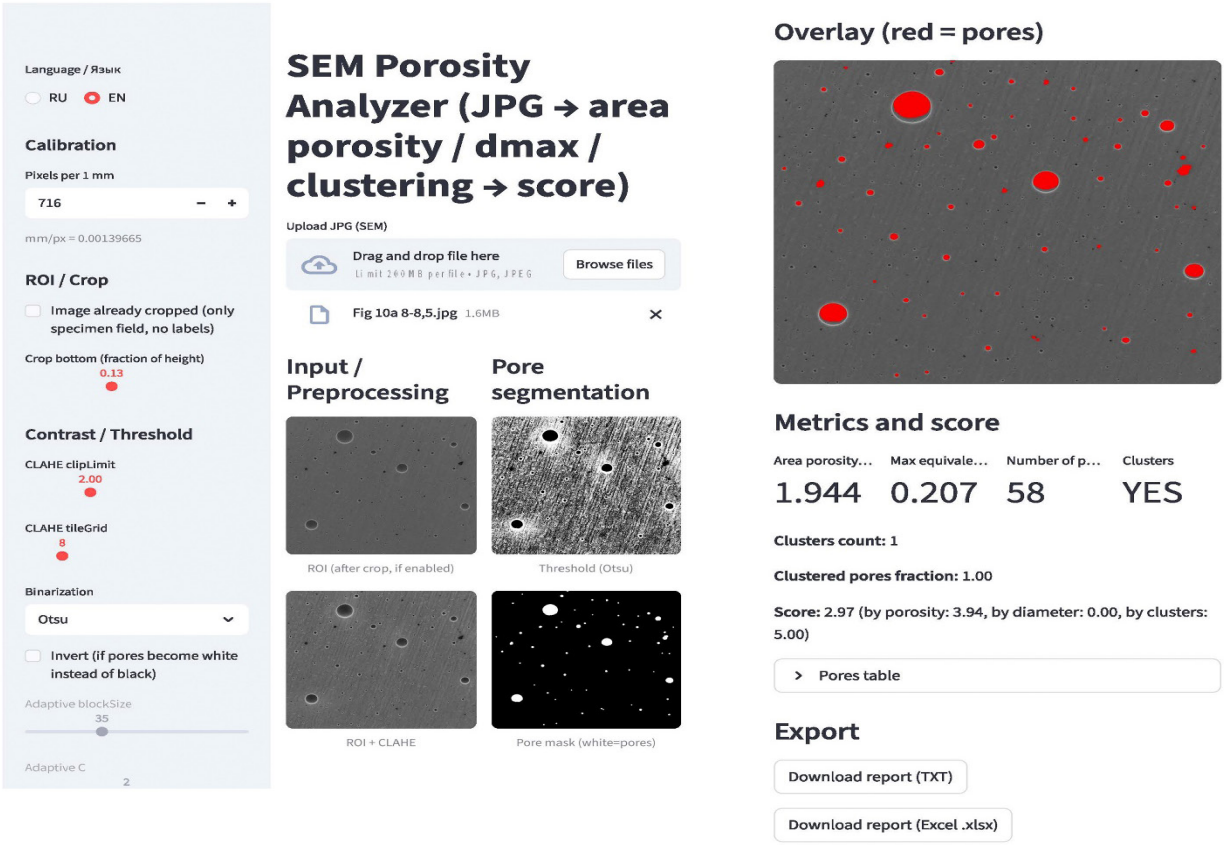


*Fig. 5.* Interface of the developed *SEM Porosity Analyzer* software during processing of sample 12–5

The upper part of the sidebar contains a calibration block, where the number of pixels corresponding to 1 mm is specified (for specimen 12-5, the calibration is 1 mm = 716 px). Based on the entered value, the program automatically calculates the mm/px conversion coefficient, which is then used to convert all linear pore dimensions from pixels to millimeters.

The next panel block is "*ROI*". This block is designed to exclude the service area of the SEM image (inscriptions, scale bar, shooting parameters). The user can indicate that the image is already cropped (only the specimen field is used), or specify a cropping fraction from the bottom. This ensures analysis of exclusively the material area without the influence of graphic elements not related to the specimen structure.

The "*Contrast / Threshold*" block includes contrast enhancement and binarization parameters. To stabilize pore detection under non-uniform illumination, local contrast enhancement (*CLAHE*) is applied, controlled by *clipLimit* and *tileGrid* parameters. Next, the binarization method is selected: *Otsu* (automatic global threshold) or *Adaptive* (local binarization with window size and offset parameters). Additionally, an inversion toggle is provided, allowing correct processing of cases where pores are visually highlighted in the "wrong" color after binarization. The segmentation logic is based on the fact that pores in *SEM* images usually appear darker than the material matrix.

The "*Mask Cleaning*" block specifies binary mask post-processing parameters: minimum pore area (small noise cutoff) and radii for morphological closing/opening operations, which are used to smooth pore boundaries and remove individual artifacts. Adjusting this block enables stable segmentation under varying surface textures and noise levels in the image.

The "*Clustering*" block contains parameters for detecting local pore accumulations. In the implemented methodology, a cluster is defined as at least three pores within a 0.5 mm radius. This rule corresponds to the *DBSCAN* algorithm settings (*eps*, *min_samples*) and can be modified by the user if necessary. The output of this block includes determination of cluster presence, their quantity, and calculation of the pore fraction belonging to clusters (used in calculating the integral defect severity score).

The main window area sequentially displays: *ROI* images (after cropping), image after contrast enhancement (*CLAHE*), binarization result (*threshold*), pore mask, and mask overlay on the original image (pores highlighted in red for visual verification). Below is displayed the "*Metrics and Score*" panel, including: area porosity *P*, maximum equivalent pore diameter *d_max*, pore count, cluster presence, and the final integral score (with display of individual component contributions). Additionally, an expandable table is available containing parameters for each pore (area, equivalent diameter, centroid coordinates, cluster membership). At the end of the window, an "*Export*" block is placed, allowing report export to *TXT* and *Excel* formats (*Summary* sheet with processing parameters and summary metrics, *Pores* sheet with line-by-line pore data).

To enhance segmentation robustness to noise, the binary pore mask underwent morphological cleaning: small objects with areas below a specified threshold were removed, followed by closing and opening operations with a structuring element radius set by the user, to smooth pore boundaries and suppress individual artifacts. This is particularly relevant for reducing noise from machining marks during specimen preparation.

Quantitative porosity assessment was performed on the cleaned binary mask obtained from pore segmentation within the region of interest (*ROI*). The area fraction of pores *P*, %, was determined as the ratio of the number of pixels assigned to pores to the total number of pixels in the *ROI*:

$$P = 100 \cdot \frac{N\_pore}{N\_all}, \tag{4}$$

where *N_pores* is the number of pixels corresponding to pores; *N_total* is the total number of pixels in the *ROI*.

For each pore as a connected region of the binary mask, geometric characteristics were calculated (area, centroid coordinates, equivalent diameter). The equivalent diameter *d_eq* was determined from the pore area *A*:

$$d\_eq = 2 \cdot \sqrt{\frac{A}{\pi}}, \tag{5}$$

Linear dimensions were recalculated from pixels to millimeters using the mm/px calibration coefficient. The maximum equivalent pore diameter *d_max* was taken as the maximum *d_eq* value among all pores detected within the *ROI*. Pore clustering was evaluated based on pore centroid coordinates (in mm) using the *DBSCAN* method. A cluster was defined as a local accumulation of at least three pores within a 0.5 mm radius (algorithm parameters: *eps* = 0.5 mm; *min_samples* = 3). For quantitative interpretation, the *C* indicator was calculated — the fraction of pores belonging to clusters:

$$C = \frac{n\_p,cl}{N}, \tag{6}$$

where *n_p,cl* is the number of pores assigned by the *DBSCAN* algorithm to clusters (label ≠ –1); *N* is the total number of pores in the *ROI*.

The integral (decimal) defect severity assessment was formed based on three partial indicators: porosity *S_P*, maximum diameter *S_d*, and clustering *S_C*. The partial scores *S_P* and *S_d* were determined according

to the thresholds in Table 2 with linear interpolation within each interval (for *P*: 0.05; 0.5; 1.0; 2.0; 4.0%; for *d_max*: 0.30; 0.50; 1.00; 1.50; 2.00 mm). The clustering component was converted to a 0–5 scale according to the following relationship:

$$S\_C = 5 \cdot \sqrt{C}, \quad (7)$$

The final score *S* was calculated as the weighted sum of the partial components with weighting coefficients of 0.5/0.3/0.2:

$$S = 0.5 \cdot S\_P + 0.3 \cdot S\_d + 0.2 \cdot S\_C, \quad (8)$$

To maintain a conservative acceptance logic, when rejection threshold values were reached, $S = 5$ was assigned for $P > 4\%$ or $d\_max > 2.0$ mm.

## Results and discussion

At the first stage, the study was aimed at selecting a vibration regime that ensures maximum *MPCM* fluidity during mold filling, but without signs of phase separation and foaming. The assessment was based on the fixture filling time, which forms five cylindrical specimens per run. It was experimentally established [12] that a frequency of 40–60 Hz at an amplitude of 0.2–0.6 mm provides minimum filling time and, consequently, the best cavity filling while maintaining the structural stability of the composition (without visible signs of phase separation and foaming induction) [12, 13]. The specification of a range is due to the fact that the "fixture–mold–composition" system is dynamically compliant. When working with massive fixtures, fluctuations in frequency and amplitude are observed due to natural vibrations, changes in mass and material distribution, as well as background mechanical noise. Within each series of experiments, the parameters were controlled and remained within the specified range. The influence of these fluctuations is accounted for in the statistical assessment of result reproducibility.

From a technological perspective, this is particularly important for *MCT* tool bodies: filling of internal cavities in thin-walled *SLM* shells occurs under conditions of limited supply channel cross-sections, presence of local "pockets", and zones of increased air entrapment risk (including near the shell wall and adjacent to *CLTM* channels). Therefore, the vibration regime was subsequently fixed as constant, and the vacuum level was taken as the variable factor in the second stage.

At the second stage, the pattern of *MPCM* gas porosity variation was determined depending on the pressure in the vacuum chamber with constant vibration parameters (40–60 Hz; 0.2–0.6 mm). Pore formation during vacuum infusion is caused by air entrapment, volatile release, and impregnation front features. These mechanisms are analyzed in detail in void formation models. For epoxy systems, the contribution of volatile-induced pores is separately identified, and approaches to their suppression by changing vacuuming regimes and pressure stages are shown. The pressure range covered conditions from atmospheric to deep vacuum of 101,325–50 Pa, with larger steps used in the "low vacuum" zone, and a 50 Pa step in the operating value range ($\boldsymbol{p} \leq 600$ Pa).

The variation scheme was as follows:

– in the high pressure region (low vacuum), larger steps were used: 101,325; 5,000; 2,000; 1,000; 800 Pa;

– in the "operating" vacuum value range ($\boldsymbol{p} \leq 600$ Pa), the pressure change step was 50 Pa: 600; 550; 500; 450; 400; 350; 300; 250; 200; 150; 100; 50 Pa.

Fig. 6–13 show the microscopy results of the corresponding specimens obtained at various residual pressure values.

The results are summarized in Table 4, which was compiled based on the mean porosity score values from five specimens for each regime (five specimens were evaluated in each experiment).

According to the data in Table 2, three characteristic behavior regions were identified:

– high pressures (ineffective degassing) (101,325–2,000 Pa). At atmospheric pressure and at $\boldsymbol{p}$ on the order of several thousand pascals, developed porosity is observed: large pores, clusters, uneven distribution; the mean porosity score remains high (for example, 4.5 points at 101,325 Pa, 3.8 points at 5,000 Pa, 3.2 points at 2,000 Pa), and the material is deemed unsuitable for critical filling of *MCT* tool bodies.

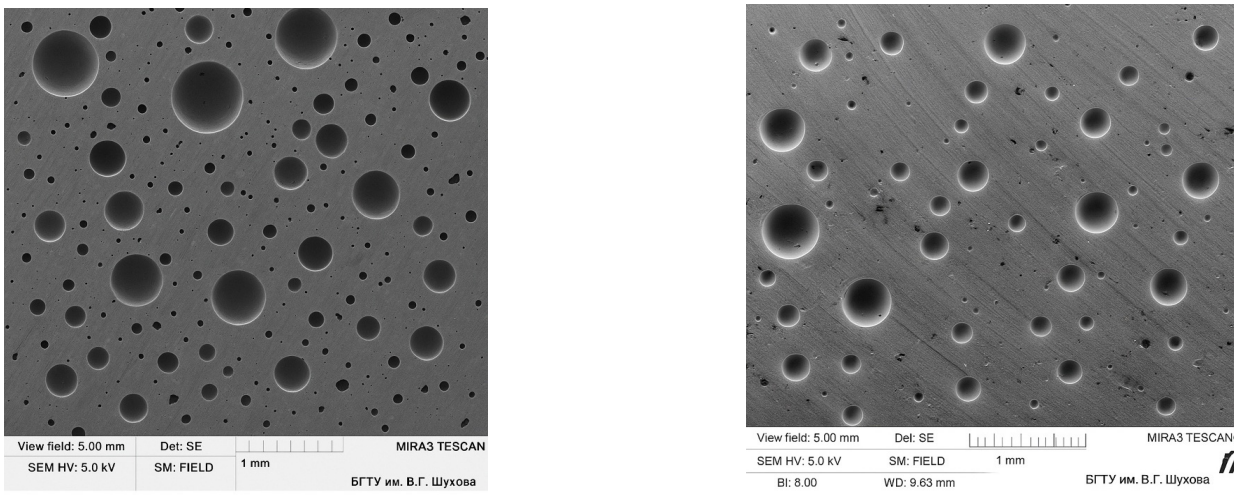


*a* *b*

*Fig. 6.* Microscopy image of *MPCM* samples:

*a* – Degassing pressure 5,000 Pa; *b* – degassing pressure 2,000 Pa

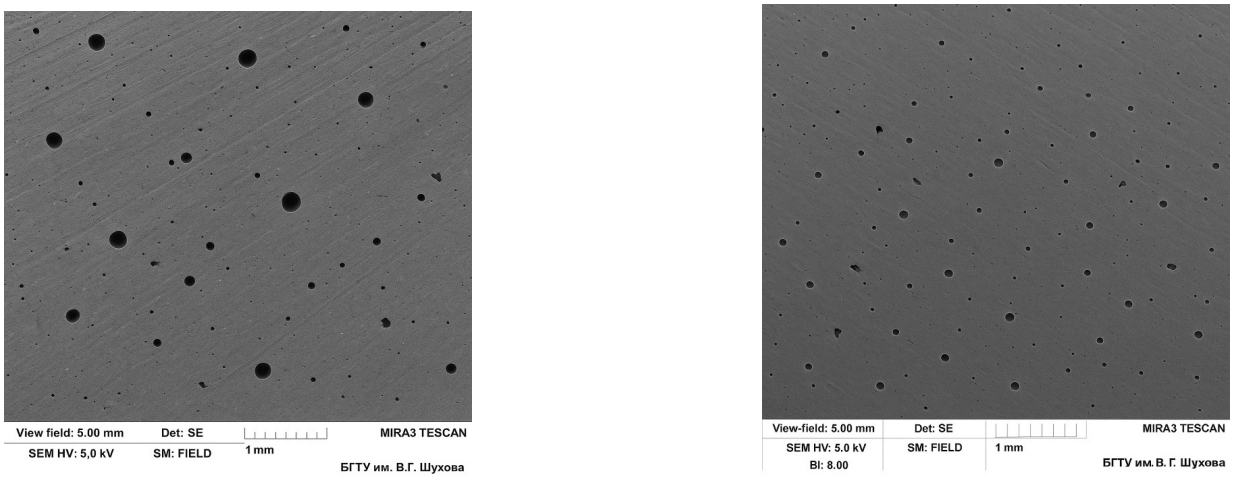


*a* *b*

*Fig. 7.* Microscopy image of *MPCM* samples:

*a* – Degassing pressure 1,000 Pa; *b* – degassing pressure 800 Pa

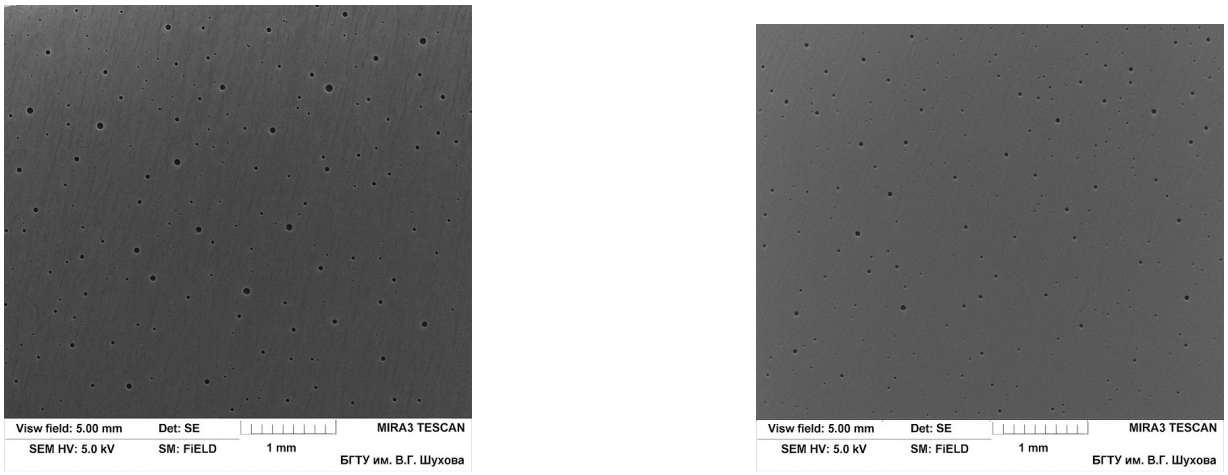


*a* *b*

*Fig. 8.* Microscopy image of *MPCM* samples:

*a* – Degassing pressure 600 Pa; *b* – degassing pressure 550 Pa

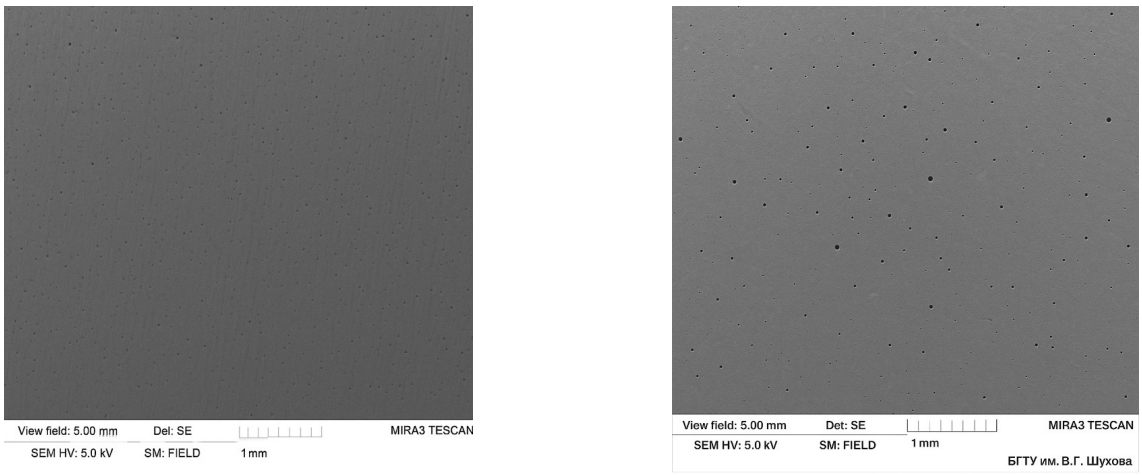


*a* *b*

*Fig. 9.* Microscopy image of *MPCM* samples:
*a* – Degassing pressure 500 Pa; *b* – degassing pressure 450 Pa

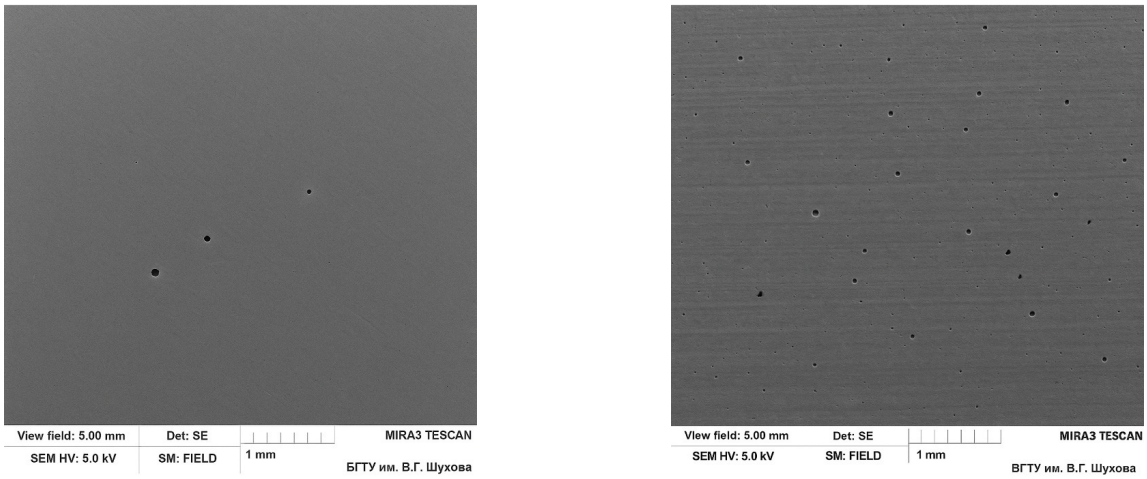


*a* *b*

*Fig. 10.* Microscopy image of *MPCM* samples:
*a* – Degassing pressure 400 Pa; *b* – degassing pressure 350 Pa

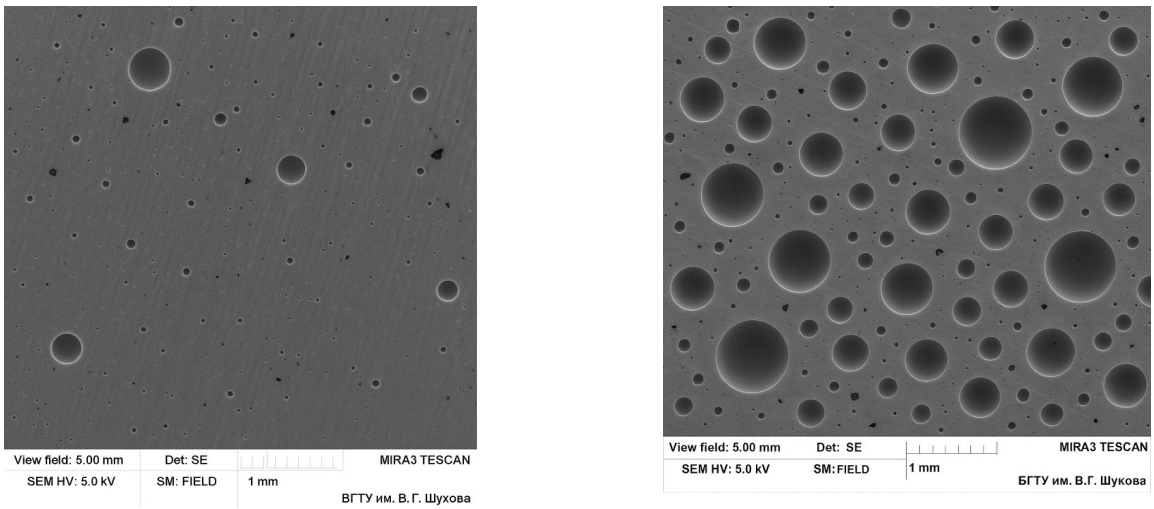


*a* *b*

*Fig. 11.* Microscopy image of *MPCM* samples:
*a* – Degassing pressure 300 Pa; *b* – degassing pressure 250 Pa

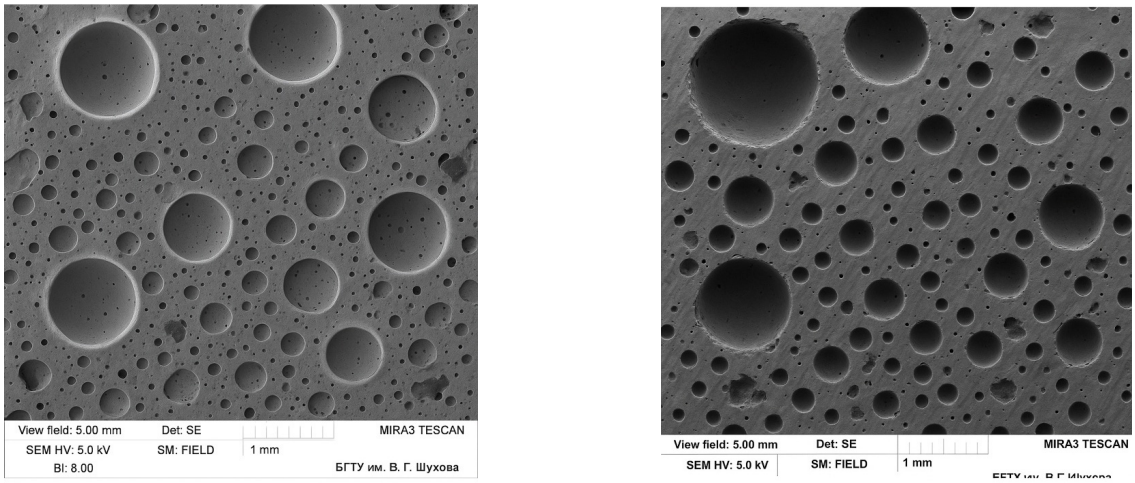


*a* *b*

*Fig. 12.* Microscopy image of *MPCM* samples:

*a* – Degassing pressure 200 Pa; *b* – degassing pressure 150 Pa

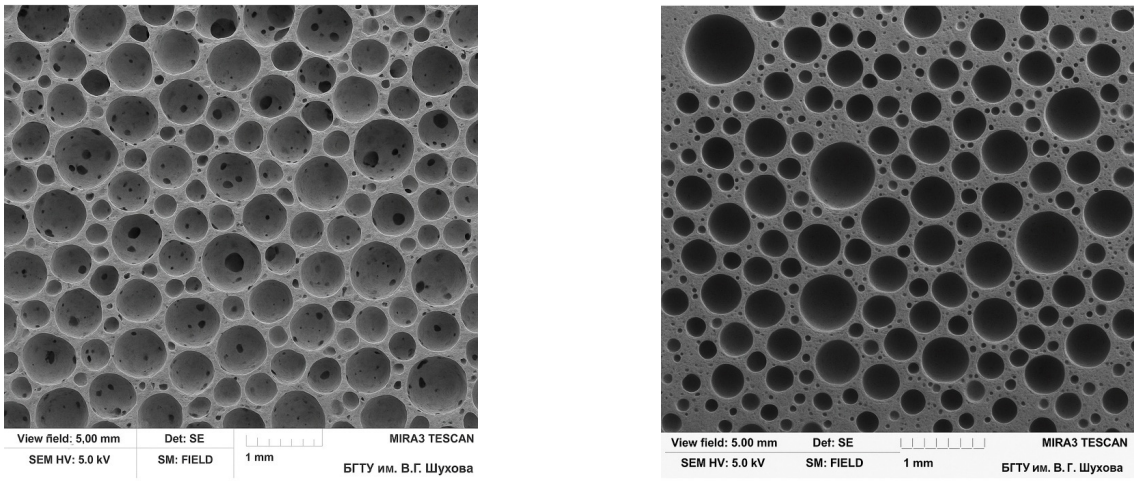


*a* *b*

*Fig. 13.* Microscopy image of *MPCM* samples:

*a* – Degassing pressure 100 Pa; *b* – degassing pressure 50 Pa

Table 4

**Influence of the vacuum level during degassing on the scoring of the porosity of *MPCM***

| Exp. No. | Degassing pressure, *p* (Pa) | Porosity character | Mean score | Acceptance assessment | Sample porosity score | | | | | Δ95 |
|---|---|---|---|---|---|---|---|---|---|---|
| | | | | | 1 | 2 | 3 | 4 | 5 | |
| 1 | 101325 | Large pores, clusters, uneven distribution | 4.5 | Not acceptable | 5.0 | 3.8 | 4.3 | 4.6 | 4.8 | 0.58 |
| 2 | 5000 | Developed porosity, individual clusters | 3.8 | Not acceptable | 5.0 | 3.5 | 3.5 | 3.5 | 3.5 | 0.83 |
| 3 | 2000 | Medium-sized pores, porosity reduced but still significant | 3.2 | Not acceptable | 5.0 | 2.7 | 2.7 | 2.8 | 2.8 | 1.25 |
| 4 | 1000 | Dispersed and medium pores, clustering decreases | 2.7 | Conditionally acceptable | 2.4 | 3.3 | 2.6 | 2.6 | 2.6 | 0.43 |
| 5 | 800 | Mostly fine pores, isolated larger ones | 2.3 | Conditionally acceptable | 2.1 | 2.7 | 2.3 | 2.1 | 2.3 | 0.30 |
| 6 | 600 | Dispersed fine pores without pronounced | 2.1 | Conditionally acceptable | 1.8 | 2.3 | 2.2 | 2.1 | 2.1 | 0.30 |
| 7 | 550 | Fine pores, uniform distribution | 2.0 | Conditionally acceptable | 1.7 | 2.3 | 2.1 | 1.9 | 2.0 | 0.28 |

The End Table 4

| Exp. No. | Degassing pressure, *p* (Pa) | Porosity character | Mean score | Acceptance assessment | Sample porosity score | | | | | Δ95 |
|---|---|---|---|---|---|---|---|---|---|---|
| | | | | | 1 | 2 | 3 | 4 | 5 | |
| 8 | 500 | Fine dispersed porosity | 1.9 | Acceptable | 1.6 | 2.2 | 1.9 | 1.8 | 2.0 | 0.25 |
| 9 | 450 | Fine pores, no clusters | 1.8 | Acceptable | 1.5 | 2.1 | 1.8 | 1.7 | 1.9 | 0.24 |
| 10 | 400 | Isolated fine pores, practically no clusters | 1.2 | **Optimal** | 0.9 | 1.7 | 1.1 | 1.3 | 1.2 | 0.37 |
| 11 | 350 | Dispersed porosity, isolated pores | 1.5 | **Optimal** | 1.3 | 1.7 | 1.5 | 1.6 | 1.4 | 0.12 |
| 12 | 300 | Onset of "ebullition" (boiling), pore coarsening, local clusters | 3.0 | Not acceptable | 2.3 | 3.5 | 3.2 | 3.1 | 2.9 | 0.59 |
| 13 | 250 | Large pores, foaming, pronounced clustering | 3.5 | Not acceptable | 5.0 | 3.1 | 3.1 | 3.1 | 3.2 | 1.04 |
| 14 | 200 | Developed foaming, large voids | 4.0 | Not acceptable | 5.0 | 3.7 | 3.7 | 3.8 | 3.8 | 0.70 |
| 15 | 150 | Pronounced microporosity | 4.3 | Not acceptable | 5.0 | 3.8 | 4.0 | 4.3 | 4.4 | 0.57 |
| 16 | 100 | Large cavities, structural heterogeneity | 4.6 | Not acceptable | 5.0 | 4.2 | 4.4 | 4.6 | 4.8 | 0.39 |
| 17 | 50 | Severe foaming, continuous gas regions | 5.0 | Not acceptable | 5.0 | 5.0 | 5.0 | 5.0 | 5.0 | 0.00 |

2. Operating region with monotonic porosity reduction (1,000–450 Pa). When transitioning to deeper vacuum, the mean porosity score steadily decreases: at 1,000 Pa – 2.7; at 800 Pa – 2.3; at 600 Pa – 2.1; at 500 Pa – 1.9; at 450 Pa – 1.8. Qualitatively, this corresponds to a transition from dispersed/medium pores with residual clustering to fine dispersed porosity without clusters, which is already acceptable for filling *SLM* shell cavities.

3. Optimum and "boiling" region (400–50 Pa). Minimum porosity is achieved at $\boldsymbol{p}$ = 400–350 Pa, where the mean score is 1.2–1.5, and the regime is qualified as optimal (Table 2). However, upon further pressure reduction to $\boldsymbol{p} \leq 300$ Pa, a qualitative transition is recorded: intensive "boiling" of the composition and foaming begin, accompanied by a sharp increase in porosity (for example, 3.0 points at 300 Pa, 3.5 at 250 Pa, 4.0 at 200 Pa, up to 5.0 points at 50 Pa).

In addition to the scoring assessment, the area fraction of pores ***P***, % was calculated from binarized *SEM* images, and pore size characteristics (equivalent diameter) were evaluated. Quantitative values of ***P***, % for key regimes (optimal region, boundary region, and foaming region at $\boldsymbol{p} \leq 300$ Pa) are presented in Table 5 and confirm the conclusions obtained from the scoring scale.

Table 5

**Quantitative porosity metrics of *MPCM* from *SEM* image analysis**

**(area fraction of pores and pore size characteristics)**

| Sample No. | *p* (Pa) | *P* (%) (Mean) | Δ95, % | *d_eq* (μm) (Median) | d_eq (μm) (P10–P90) | *N_pores* (1/mm²) |
|---|---|---|---|---|---|---|
| 4 | 1,000 | 1.45 | 0.35 | 170 | 55–520 | 105 |
| 10 | 400 | 0.32 | 0.10 | 55 | 20–140 | 140 |
| 12 | 300 | 2.40 | 0.60 | 260 | 70–1,300 | 65 |

Thus, the experiment confirms the "*V*-shaped" pattern: as vacuum depth increases from atmospheric to approximately 450 Pa, porosity decreases, but under excessive vacuum below 300 Pa, the material transitions into a foaming and microporosity regime. Under these conditions, the increase in defect severity is primarily due to the growth of characteristic pore sizes and the expansion of the equivalent diameter ***d_eq*** range, as well as the appearance of clusters, accompanied by an increase in the area fraction of pores ***P***. At the same time, the density of individual pores ***N_pores*** may decrease due to the merging of small pores into larger defects.

The observed *V*-shaped dependence of porosity on residual pressure during vibro-vacuum degassing can be interpreted as the result of competition between two mechanisms acting in opposite directions. At relatively high pressures (low vacuum), incomplete removal of the gas phase dominates, whereas under too deep vacuum, secondary pore generation (foaming) and defect severity increase are intensified.

The gas phase in the analyzed metal–polymer system has a mixed nature and may include: entrapped air (introduced during mixing/stirring and casting); dissolved gases (primarily air dissolved in the polymer matrix before curing); volatile components; moisture (adsorbed on the filler and fixture walls); gaseous reaction products (possible locally as a consequence of side processes and/or interaction with moisture, especially at the early curing stage).

In the "low vacuum" region, the degassing driving force is small: the chamber pressure does not sufficiently reduce gas solubility and does not ensure active bubble rise. The viscosity of the composition (enhanced by high filler content) additionally limits bubble rise and coalescence, so part of the gas phase is fixed in the volume, forming porosity after curing.

Upon further pressure reduction ($\boldsymbol{p} \leq 300$ Pa), the opposite mechanism is activated: a sharp drop in external pressure leads to intensive nucleation and bubble growth. This may be associated with reaching or approaching the saturated vapor pressure of present volatile components at 20–25 °C or with rapid release of dissolved gases upon reduced solubility. The presence of a large number of nucleation sites ("filler–matrix" boundaries, micro-irregularities, local inhomogeneities) contributes to multiple bubble nucleation and the formation of fine-dispersed porosity. As a result, under too deep vacuum, the contribution of "secondary pore generation" begins to exceed the effect of primary gas removal, which leads to an increase in defect severity on the right branch of the *V*-shaped curve.

The region around 400 Pa corresponds to a compromise: the pressure is already low enough to effectively expand and remove primarily entrapped bubbles and reduce dissolved gas, but not yet low enough for the mass initiation of intensive bubble nucleation throughout the volume. This is consistent with the fact that at this pressure, the minimum porosity score and the most favorable pore morphology are achieved.

The obtained dependence shape and the presence of an optimal vacuum level qualitatively agree with data provided for degassing of reactive epoxy systems: in works devoted to vacuum degassing of resins [8, 10], it is emphasized that excessive pressure reduction does not always lead to further quality improvement, since under too deep vacuum, foaming and porosity growth are possible due to evaporation of volatile components and intensive release of dissolved gases. Unlike low-viscosity epoxy resins, the studied MPCM composition is highly filled and significantly more viscous; therefore the pressure optimum may shift and become more pronounced: on one hand, the "resistance" to bubble rise increases, on the other hand, the number of nucleation sites at phase boundaries increases. These features explain both the presence of a pronounced porosity minimum at intermediate pressure and the increase in defect severity under excessively deep vacuum.

Analysis of micrographs (Fig. 6–13) shows that when degassing pressure changes, not only the integral defect severity score changes, but also the pore morphology. In the low vacuum region, relatively large single pores and extended defects predominate, which corresponds to incomplete removal of primarily entrapped air. The pores exhibit more pronounced size variability, and local clusters are encountered. When transitioning to the optimal pressure of approximately 400 Pa, the "cleanest" structure is observed, with both the area fraction of pores and the fraction of large defects decreasing. The pore size distribution shifts toward smaller ***d_eq*** values, and the pores become more isolated (clustering tendency decreases). Upon further pressure reduction ($\boldsymbol{p} \leq 300$ Pa), the structure changes to the opposite: fine-dispersed porosity forms with a large number of pores per unit area, which corresponds to intensive nucleation and bubble growth throughout the volume (foaming). Quantitatively, this manifests as an increase in pore density and a change in the equivalent diameter distribution, accompanied by simultaneous deterioration of the total defect severity.

It should be noted that within the framework of this study, the inter-operator reproducibility of the scoring scale was not evaluated (assessment was performed by a single operator), nor was statistical validation of the scale conducted based on correlation with quantitative porosity parameters (*P*, %, *d_eq* characteristics). The specified validations will be performed in further studies.

A graphical interpretation of the obtained dependence is presented in Fig. 14.

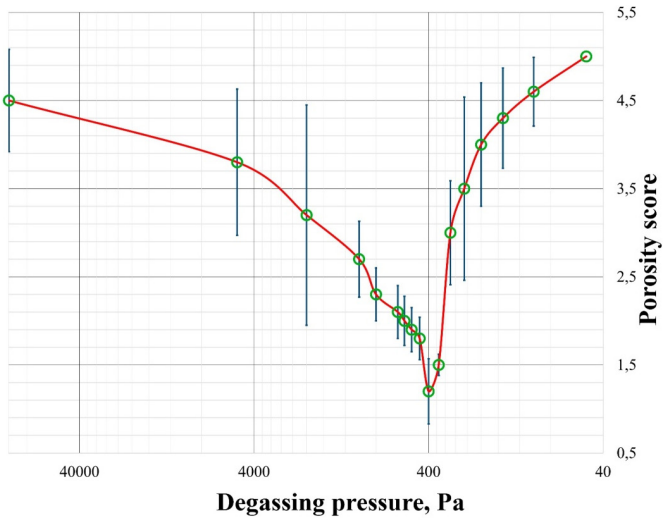


*Fig. 14.* Dependence of the *MPCM* porosity score on degassing pressure

From a practical standpoint, the observed dependence is directly explained by the competition between two mechanisms. Under insufficient vacuum (high pressures), the removal of dissolved and entrapped air is limited; bubbles persist and coalesce into clusters. For *MCT* tool bodies, this is critical: pores near the thin-walled *SLM* shell wall and adjacent to *CLTM* channels form local filling defects, degrade thermal conductivity, and create zones of inhomogeneous stiffness, which reduces property reproducibility and increases the risk of defects during subsequent tool operation. Under excessively deep vacuum, the composition transitions to an active gas evolution regime, leading to pore coarsening and increased microporosity. In technological terms, this means that the attempt to "increase vacuum strength" beyond a certain threshold becomes counterproductive: instead of degassing, foaming occurs along with the formation of large gas regions, which is unequivocally unacceptable according to acceptance criteria. The obtained *V*-shaped dependence of porosity on residual pressure agrees with conclusions by other authors regarding the existence of an optimal vacuum level during degassing of reactive systems [18–22].

The experimentally established optimal range of 400–350 Pa represents a compromise: it ensures minimum porosity according to the adopted scale (1–2 points) without the foaming effect, and is therefore recommended for technological application in the manufacturing of *MCT* cutting tool bodies.

Based on the experiment, recommended degassing regimes using the vibro-vacuum setup were formulated: vacuum depth of approximately 400 Pa, holding time at the specified residual pressure of 5 minutes (time counted after reaching and stabilizing the pressure), and composition temperature of 20–25 °C. The time required to reach the regime and stabilize pressure in the vacuum chamber was 3–7 minutes and was not included in the 5-minute holding time.

## Conclusion

In this study, the effect of residual pressure during vibro-vacuum degassing on *MPCM* gas porosity was experimentally investigated, and a technologically preferable vacuum range was determined for application in *MCT* cutting tool bodies. The obtained results enable the development of a reproducible control methodology and practical recommendations for small-scale production conditions.

1. A porosity evaluation methodology and *MPCM* acceptance criteria were adapted for *MCT* tool bodies: a microdefect rating scale was introduced, and *SEM* microscopy with automated image processing was standardized, ensuring series comparability and assessment reproducibility.

2. A series of experiments was conducted at various residual pressure values with production of parallel specimens ($\boldsymbol{n} = 5$ for each regime) and statistical processing of results (mean value, 95% *CI*), which ensured correct comparison of degassing regimes.

3. The "pressure–porosity" pattern was established, and optimal and critical parameter regions were determined: minimum porosity is achieved at $\boldsymbol{p}$ approximately 400–350 Pa, whereas at $\boldsymbol{p} \leq 300$ Pa, foaming and increased defect severity are observed. On this basis, a technologically preferable vacuum range and technological limitations for filling *MCT* tool bodies *SLM* shells were justified.

4. The holding time parameters of 5 min after pressure stabilization and composition temperature of 20–25 °C were not varied in this study and were used as fixed experimental conditions; therefore, they are provided as working technological parameters recommended based on technological experience, whereas the experimentally justified factor in this series is the residual pressure range.

## References

1. Kelliger T., Meurer M., Bergs T. Potentials of additive manufacturing for cutting tools: a review of scientific and industrial applications. *Metals*, 2024, vol. 14 (9), p. 982. DOI: 10.3390/met14090982.

2. Kugaevskii S.S., Gamberg A.E., Kulpina K.A. Development of modular lathe cutter with the application of additive technologies. *Proceedings of the 6th International Conference on Industrial Engineering (ICIE 2020)*, Chelyabinsk, Russia, May 18–22, 2020. Springer, 2021, pp. 114–122. DOI: 10.1007/978-3-030-54814-8_14.

3. Lubimyi N.S., Chepchurov M., Polshin A.A., Gerasimov M.D., Chetverikov B.S., Chetverikova A., Tikhonov A.A., Maltsev A. Reducing the cost of 3D metal printing using selective laser melting (SLM) technology in the manufacture of a drill body by reinforcing thin-walled shell forms with metal-polymers. *Journal of Manufacturing and Materials Processing*, 2024, vol. 8 (2), p. 44. DOI: 10.3390/jmmp8020044.

4. Al-Sulaiman F., Mokheimer E., Al-Nassar Y. Prediction of the thermal conductivity of the constituents of fiber-reinforced composite laminates. *Heat and Mass Transfer*, 2006, vol. 42, pp. 370–377. DOI: 10.1177/0021998305055548.

5. Ljubimyj N.S., Chepchurov M.S., Chetverikov B.S., Tabekina N.A., Evtushenko E.I. Technological heredity in the manufacture of metallopolymeric build-forming molds. *ARPN Journal of Engineering and Applied Sciences*, 2016, vol. 11 (20), pp. 12302–12310.

6. van Oosterom S., Schreier A., Battley M., Bickerton S., Allen T. Influence of dissolved gases in epoxy resin on resin infusion part quality. *Composites. Part A: Applied Science and Manufacturing*, 2020, vol. 132, p. 105818. DOI: 10.1016/j.compositesa.2020.105818.

7. Chen D., Arakawa K., Xu C. Reduction of void content of vacuum-assisted resin transfer molded composites by infusion pressure control. *Polymer Composites*, 2014, vol. 36 (9), pp. 1629–1637. DOI: 10.1002/pc.23071.

8. Juan J., Silva A., Tornero J., Gamez J., Salán N. Void content minimization in vacuum infusion (VI) via effective degassing. *Polymers*, 2021, vol. 13, p. 2876. DOI: 10.3390/polym13172876.

9. Meier R., Kahraman I., Seyhan A., Zaremba S., Drechsler K. Evaluating vibration assisted vacuum infusion processing of hexagonal boron nitride sheet modified carbon fabric/epoxy composites in terms of interlaminar shear strength and void content. *Composites Science and Technology*, 2016, vol. 128, pp. 94–103. DOI: 10.1016/j.compscitech.2016.03.022.

10. Yang X., Zhan L., Jiang C., Zhao X., Guan C., Chang T. Evaluating random vibration assisted vacuum processing of carbon/epoxy composites in terms of interlaminar shear strength and porosity. *Journal of Composite Materials*, 2019, vol. 53 (17), pp. 2367–2376. DOI: 10.1177/0021998319829531.

11. JSC "Metal-Polymer Materials LEO". *Technical specifications TU 2257-002-48460567-00. Metal-polymer "Ferro-chrome"*. Moscow, 2000. (In Russian). Available at: http://leopolimer.ru/ (accessed 23.03.2026).

12. Polshin A., Lubimyi N., Chetverikov B., Chepchurov M., Maltsev A., Tikhonov A. Experimental substantiation of the technology for manufacturing composite parts based on a viscous metal-polymer. *Australian Journal of Mechanical Engineering*, 2024, vol. 23 (3), pp. 488–498. DOI: 10.1080/14484846.2024.2343449.

13. Mehdikhani M., Gorbatikh L., Verpoest I., Lomov S.V. Voids in fiber-reinforced polymer composites: a review on their formation, characteristics, and effects on mechanical performance. *Journal of Composite Materials*, 2019, vol. 53 (12), pp. 1579–1669. DOI: 10.1177/0021998318772152.

14. GOST 19200–80. *Otlivki iz chuguna i stali. Terminy i opredeleniya defektov* [State standard 19200–80. Iron and steel castings. Terms and definitions of defects]. Moscow, Standards Publ., 1992. Available at: https://docs.cntd.ru/document/1200005049 (accessed 23.03.2026).

15. GOST R 56679–2015. *Kompozity polimernye. Metod opredeleniya pustot* [State standard R 56679–2015. Polymer composites. Method for determination of voids]. Moscow, Standartinform Publ., 2016. Available at: https://files.stroyinf.ru/Data2/1/4293758/4293758544.pdf (accessed 23.03.2026).

16. ISO 7822:1990(E). *Textile glass reinforced plastics – determination of void content – loss on ignition, mechanical disintegration and statistical counting methods*. Geneva, International Organization for Standardization (ISO), 1990. 9 p. Available at: https://cdn.standards.iteh.ai/samples/14740/1052bc459edd47acb887089816ec199d/ISO-7822-1990.pdf (accessed 23.03.2026).

17. Saenz-Castillo D., Martín M.I., Calvo S., Rodriguez-Lence F., Güemes A. Effect of processing parameters and void content on mechanical properties and NDI of thermoplastic composites. *Composites. Part A: Applied Science and Manufacturing*, 2019, vol. 121, pp. 308–320. DOI: 10.1016/j.compositesa.2019.03.035.

18. Lee D.H., Lee W.I., Kang M.K. Analysis and minimization of void formation during resin transfer molding process. *Composites Science and Technology*, 2006, vol. 66 (16), pp. 3281–3289. DOI: 10.1016/j.compscitech.2005.07.008.

19. Pupin C., Ross A., Dubois C., Rietsch J.-C., Vernet N., Ruiz E. Formation and suppression of volatile-induced porosities in an RTM epoxy resin. *Composites. Part A: Applied Science and Manufacturing*, 2017, vol. 94, pp. 146–157. DOI: 10.1016/j.compositesa.2016.12.006.

20. Wong D., Anwar M., Debnath S., Abdullah A.H., Izman S., Pramanik A. Degassing process influence on tensile strength of neat E132 epoxy polymeric materials. *Materials Science Forum*, 2021, vol. 1026, pp. 129–135. DOI: 10.4028/www.scientific.net/MSF.1026.129.

21. Choi J., Jung H., Han S. The effect of porosity on the thermal conductivity of highly thermally conductive adhesives. *Polymers*, 2023, vol. 15 (14), p. 3083. DOI: 10.3390/polym15143083.

22. Guo Y., Ruan K., Shi X., Yang X., Gu J. Factors affecting thermal conductivities of the polymers and polymer composites: a review. *Composites Science and Technology*, 2020, vol. 193, p. 108134. DOI: 10.1016/j.compscitech.2020.108134.

## Conflicts of Interest

The authors declare no conflict of interest.